W deposition and titanium fluoride formation during WF_6 reduction by Ti: Reaction path and mechanisms

G. Ramanath,[a] J. E. Greene, J. R. A. Carlsson, and L. H. Allen
Coordinated Science Laboratory, Materials Research Laboratory, and Department of Materials Science, University of Illinois, 1304 West Green Street, Urbana, Illinois 61801

V. C. Hornback and D. J. Allman
Symbios Logic Incorporated, 1635 Aeroplaza Drive, Colorado Springs, Colorado 80219

Reaction of WF_6 with air-exposed 27- and 250-nm-thick Ti films has been studied using Rutherford backscattering spectroscopy, scanning and high-resolution transmission electron microscopy, electron and x-ray diffraction, and x-ray photoelectron spectroscopy. We show that W nucleates and grows rapidly at localized sites on Ti during short WF_6 exposures (≈ 6 s) at 445 °C at low partial pressures $p_{WF_6} < 0.2$ Torr. Large amounts of F, up to $\approx 2.0 \times 10^{17}$ atoms/cm^2 corresponding to an average F/Ti ratio of 1.5 in a 27-nm-thick Ti layer, penetrate the Ti film, forming a solid solution and nonvolatile TiF_3. The large stresses developed due to volume expansion during fluorination of the Ti layer result in local delamination at the W/Ti and the Ti/SiO$_2$ interfaces at low and high WF_6 exposures, respectively. WF_6 exposure at $p_{WF_6} > 0.35$ results in the formation of a network of elongated microcracks in the W film which allow WF_6 to diffuse through and attack the underlying Ti, consuming the 27-nm-thick Ti film through the evolution of gaseous TiF_4. © *1999 American Institute of Physics.* [S0021-8979(99)10303-7]

I. INTRODUCTION

W chemical vapor deposition (CVD) from WF_6—the process of choice for filling high aspect ratio holes in ultralarge-scale integrated (ULSI) circuits[1–6]—requires the use of conformal TiN/Ti bilayers. TiN is used as a diffusion barrier to prevent WF_6 reaction with underlying layers,[7–10] and Ti getters interfacial oxygen from the surface of the underlayers (e.g., Al) to reduce via resistance. On substrates such as Si and SiO$_2$, Ti also serves as an adhesion promoter by reacting to form a thin TiSi$_2$ layer.[11,12]

Delamination of sputter-deposited TiN/Ti liners during W CVD is a serious problem in the fabrication of sub-0.35 μm ULSI structures.[11–14] Recently,[15–18] we showed that such delamination is caused by WF_6 diffusing through nanopipes in underdense TiN layers, injecting F into the underlying Ti layer during W nucleation, and weakening the Ti/SiO$_2$ interface. To better understand the delamination mechanism, we study the microchemical changes and phase formation occurring in the Ti layer, especially in regions of poor TiN coverage in high-aspect ratio device features where Ti is directly exposed to the incoming flux of WF_6 molecules. Developing an understanding of F penetration into Ti is also important in order to evaluate the stability of Ti when in contact with F-containing compounds such as fluorinated silicon glass (FSG), parylene, fluorinated amorphous carbon (FLAC) etc., candidate materials for low-k dielectric applications in sub-0.25 μm devices.

It is generally known that WF_6 reacts more rapidly with Ti surfaces than TiN.[19–23] However, the pathway for WF_6 reaction with Ti and the phase formation sequence are not well understood. In fact, this reaction has been addressed only perfunctorily in reports devoted to studies of other phenomena. Some researchers[24,25] have speculated on volatile TiF_4 formation while others have suggested nonvolatile TiF_3 formation.[19–23] Barber and Shenasa[24] inferred volatile fluoride formation from their Auger electron spectroscopy data, which did not contain any Ti or F peaks following WF_6 exposure of Ti. Based upon bright-field transmission electron microscopy (TEM) micrographs, Broadbent and co-workers[19,20] suggested the formation of TiF_3. However, there was no structural information presented to identify the fluoride phase formed. Yu, Ahn, and Joshi[22,23] assumed TiF_3 formation due to a large shift in the Ti $2p$ x-ray photoelectron spectroscopy (XPS) peak when a ''clean'' Ti surface was exposed to WF_6 at room temperature. Since other nonvolatile titanium fluorides[26] and oxyfluorides[27] are also known to exist and may give rise to a similar peak shift, phase identification is not conclusive in the absence of structural information.

In this article, the reaction of WF_6 with Ti is systematically examined as a function of WF_6 dose and the phase formation sequence is revealed. We show that Ti rapidly reduces WF_6, resulting in W deposition and F injection into the Ti layer. At low average F concentrations in the Ti film, C_F up to ≈ 10 at. %, a Ti–F solid solution forms. Increasing C_F results first in the formation of TiF_3 followed by the release of gaseous TiF_4. Microcracks in the deposited W overlayer not only allow incident WF_6 molecules to diffuse

[a] Permanent address: Department of Materials Science, Rensselaer Polytechnic Institute, Troy, NY 12180; electronic mail: ramanath@rpi.edu

through them and continue the attack on the Ti underlayer, but also serve as facile paths for TiF_4 evolution. The phase formation sequence is discussed based upon thermodynamic arguments and a phenomenological model is proposed.

II. EXPERIMENTAL PROCEDURE

Ti films of two different thicknesses, 27 and 250 nm, were grown at 250 °C by magnetron sputter deposition in an Applied Materials Endura HP process tool on 700-nm-thick SiO_2 layers deposited by plasma enhanced CVD on 200-mm-diam Si(001) wafers. The base pressure in the deposition chamber was 1×10^{-8} Torr. Ti deposition was carried out in Ar at 5 mTorr, yielding a deposition rate of 2.2 nm s^{-1}. All samples were exposed to air before being loaded into a Novellus Systems Concept One cold-wall CVD reactor where they were exposed to WF_6 gas at 445 °C for 6 s in an Ar/WF_6 mixture with an Ar flow rate of 12000 sccm and a total pressure of 40 Torr. The WF_6 dose was varied by changing the WF_6 partial pressure p_{WF_6} from 0.2 to 1.3 Torr.

Rutherford backscattering spectroscopy (RBS) was used to monitor compositional changes in the reacted Ti layers. The RBS probe beam consisted of 2 MeV ^{4}He$^+$ ions incident at angles between $-10°$ and $30°$ to the sample normal and the detector was set at a scattering angle of 150°. Angle-resolved RBS was used to distinguish between, and identify the location of, light elements such as O and F. The spectra were analyzed through comparisons with RUMP[28] computer simulations.

Elemental chemical-state information was obtained using XPS. The measurements were performed in a Perkin Elmer PHI 5400 system equipped with a Mg $K\alpha$ x-ray source. Elemental binding energies were calibrated using Cu and Au standards. Surface impurities such as carbon were also used as internal references. The Ti 2p peaks were deconvolved by nonlinear least-squares curve fitting using the PHI 5000 Series-electron spectroscopy for chemical analysis (ESCA) version 4.1A computer software.

Film morphology was investigated using secondary and Z-contrast scanning electron microscopy (SEM) in Hitachi S 800 and Zeiss 960 microscopes operated at 20 kV. Plan-view TEM was carried out in a Philips CM 12 microscope at 120 kV to characterize the microstructure of the Ti film prior to, and after, WF_6 exposures. Structure and morphology of phases formed were investigated using conventional and high-resolution TEM (HRTEM), electron diffraction, and x-ray diffraction (XRD). A Rigaku DMAX-III diffractometer with a monochromatic Cu $K\alpha$ X-ray source was used for the XRD measurements.

III. RESULTS

A. W nucleation and morphology

Ti films exposed to WF_6 for 6 s at various partial pressures p_{WF_6} were examined by SEM. Figure 1(a) shows a typical micrograph of a sample exposed to WF_6 at p_{WF_6} = 0.2 Torr. Spherical W particles (average size 111 $\pm$ 70 nm) form at local sites on the Ti film. The particles appear in the micrograph as spheres of bright contrast, iden-
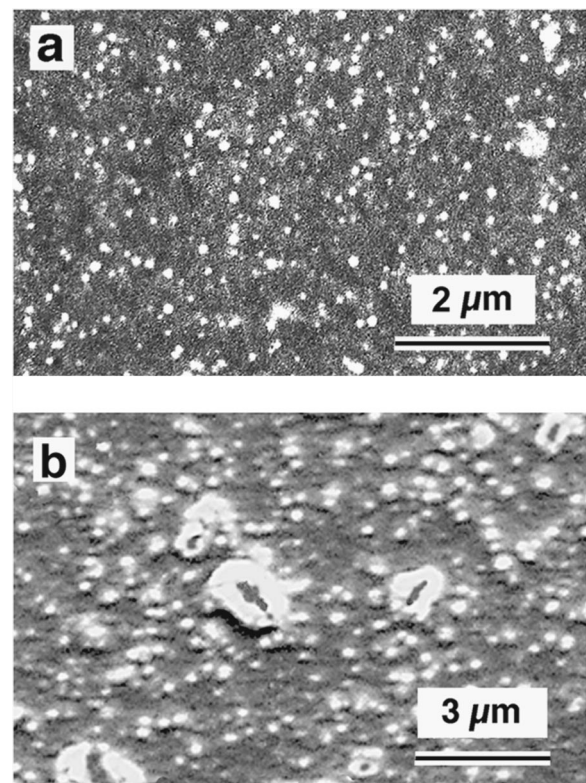

FIG. 1. SEM micrographs of Ti/SiO_2 samples exposed to WF_6 for 6 s at p_{WF_6} values of (a) 0.2, and (b) 0.35 Torr.

tified to be W by Z-contrast SEM and energy dispersive x-ray spectroscopy (EDX). Microcracks were observed in the larger W particles when p_{WF_6} was ≥ 0.35 Torr. This is clearly seen in Fig. 1(b), a representative SEM micrograph from a sample exposed to WF_6 at p_{WF_6} = 0.35 Torr. Further increases in p_{WF_6} resulted in the formation of a very rough W film with elongated microcracks extending across the film [see Fig. 2(a)]. The observed morphology is similar to that reported by Broadbent and co-workers during WF_6 reduction by $TiSi_x$.[19,20] Examination of WF_6-exposed Ti films on patterned SiO_2 substrates revealed that microcrack formation is more pronounced near the top edges of topological features such as trenches and via holes. An example is shown in Fig. 2(b).

The W overlayers exhibit local delamination even in flat areas of the sample. Examination of these regions by Z-contrast SEM (Fig. 3) and EDX revealed the presence of a thin W layer on which the spherical W particles are dispersed. The particles appear brighter than the W layer because their average diameter is much larger than the W layer thickness. These results suggest that a thin continuous W layer is deposited on Ti prior to preferential WF_6 reduction, which leads to the formation of the large W particles.

B. Fluorine incorporation and Ti etching

WF_6-exposed Ti/SiO_2 samples were analyzed by RBS in order to follow compositional changes in the Ti film as a function of partial pressure. Figure 4 shows typical RBS spectra from samples exposed to WF_6 for 6 s at p_{WF_6} values
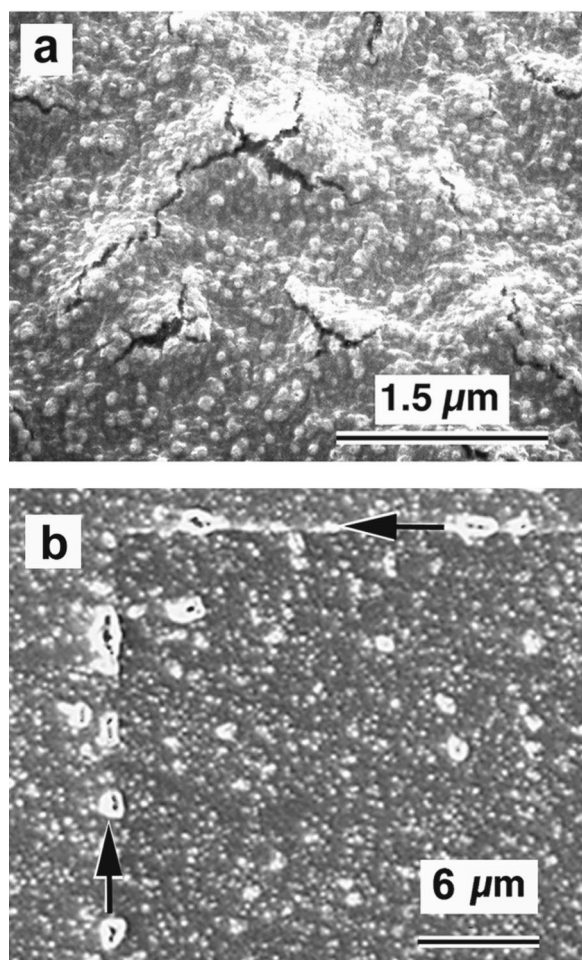
J. Appl. Phys., Vol. 85, No. 3, 1 February 1999

Ramanath *et al.*   1963

FIG. 2. (a) SEM micrograph of a Ti/SiO$_2$ sample exposed to WF$_6$ for 6 s at $p_{WF_6} = 1.3$ Torr. (b) SEM micrograph showing enhanced W growth and delamination near edges of topological features (indicated by arrows) in a Ti film deposited on a patterned SiO$_2$ substrate. This sample was exposed to WF$_6$ at $p_{WF_6} = 0.35$ Torr.

between 0 and 0.55 Torr. The O peak at ≈ 0.77 MeV in the as-deposited sample results from a 7-nm-thick native oxide on the Ti film, while the roughness of the W overlayer gives rise to the tail in the trailing edge of the W peak. RUMP
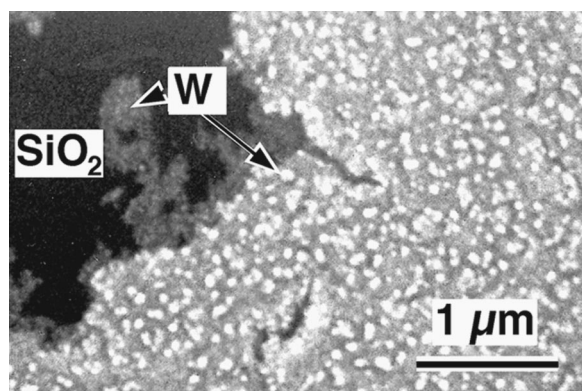

FIG. 3. Z-contrast SEM micrograph obtained by imaging the back-scattered electron intensity from a delaminated area of a Ti/SiO$_2$ sample exposed to WF$_6$ for 6 s at $p_{WF_6} = 1.3$ Torr. W appears bright against the dark background of SiO$_2$. No Ti was detected by EDX.

simulations revealed that the large peaks at ≈ 0.90 MeV superimposed on the Si substrate signal in the WF$_6$-exposed samples correspond to $\approx 2.0 \times 10^{17}$ and 8.0×10^{16} atoms/cm^2 F in the Ti layers with $p_{WF_6} = 0.20$ and 0.55 Torr, respectively. This peak is absent in the as-deposited Ti/SiO$_2$ sample, and is easily distinguished from the surface O peak by comparing angle-resolved RBS spectra.

W, Ti, and F concentrations obtained by fitting RBS spectra using RUMP simulations are plotted as a function of p_{WF_6} in Fig. 5. The nominal thickness of each layer was estimated assuming theoretical density. The W film thickness was found to increase monotonically with p_{WF_6} while the Ti thickness initially decreased by ≈ 3 nm at $p_{WF_6} = 0.2$ Torr and remained relatively unchanged for WF$_6$ exposures up to $p_{WF_6} = 0.35$ Torr. Further increases in p_{WF_6} from 0.35 to 1.3 Torr resulted in the Ti thickness decreasing sharply from 24 to ≈ 0.13 nm, indicating that Ti is rapidly etched at high WF$_6$ exposures. The consumption of the Ti film at high p_{WF_6} is illustrated by the RBS spectra in Fig. 6 which shows that the integrated Ti peak intensity in samples exposed to WF$_6$ at $p_{WF_6} = 1.3$ Torr is about two orders of magnitude lower than the corresponding intensity measured for the 27-nm-thick Ti layer in the as-deposited sample. Note the presence of the W film despite the removal of the Ti underlayer. This observation is also supported by the SEM micrograph shown in Fig. 3.

The total amount of incorporated F is not a strong function of p_{WF_6} below 1.3 Torr, the WF$_6$ partial pressure at which the F peak disappears completely. However, the F/Ti ratio increases gradually from 1.5 to 2.4 as p_{WF_6} is increased from 0.2 to 0.55 Torr. From the simultaneous loss of F and Ti at high WF$_6$ partial pressures, it is evident that F is present predominantly in the Ti layer rather than in the W overlayer.

The F/W ratio, calculated from the RBS data in Fig. 5, is 6 ± 0.7 at $p_{WF_6} < 0.35$ Torr indicating that at low WF$_6$ exposures essentially all F atoms from dissociated WF$_6$ molecules react and diffuse into the bulk of the Ti film. As p_{WF_6} increases to 0.55 Torr, the F/W ratio decreases to $\approx 3(\pm 1)$ suggesting the evolution of F-containing volatile product species.

C. TiF$_3$ formation

The above results show that gaseous titanium fluoride is not a major reaction product at $p_{WF_6} < 0.35$ Torr as evidenced by the relatively small Ti loss compared to the rapid Ti removal observed at higher WF$_6$ exposures. A combination of TEM, XRD, and XPS was used to investigate nonvolatile phase formation in WF$_6$-exposed Ti/SiO$_2$ samples with $p_{WF_6} < 0.35$ Torr.

Figure 7(a) is a representative HRTEM micrograph from a Ti/SiO$_2$ sample exposed at $p_{WF_6} = 0.2$ Torr. The presence of ≈ 20-nm-sized domains of a second phase dispersed in the Ti matrix is clearly revealed. A magnified view of a second phase domain is shown in Fig. 8. The interplanar separations and orientation of the lattice planes are consistent with the
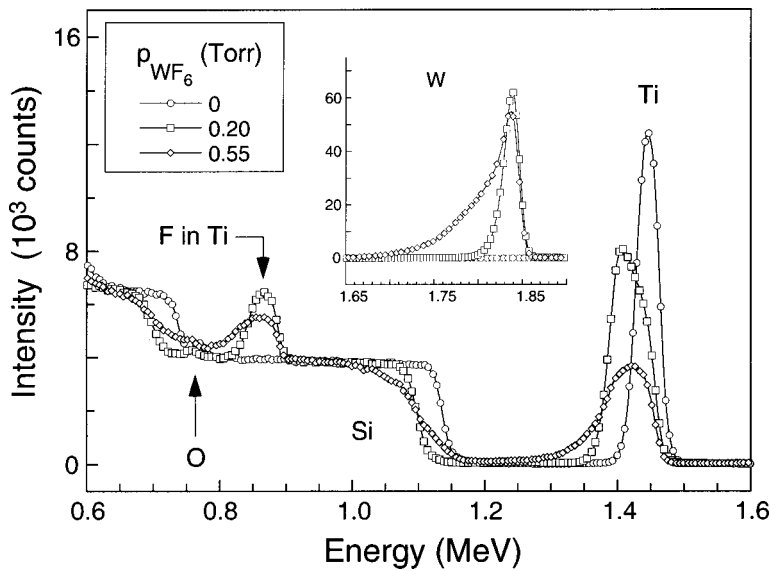
FIG. 4. Typical RBS spectra from Ti/SiO$_2$ samples exposed to WF$_6$ at p_{WF_6} between 0 and 0.55 Torr.

(01$\bar{1}$2), (10$\bar{1}$4), and (1$\bar{1}$02) planes of hexagonal TiF$_3$ (Ref. 29), as viewed along the [20$\bar{1}\bar{1}$] zone axis. Selected-area electron diffraction (SAED) patterns showing azimuthally continuous (01$\bar{1}$2), (02$\bar{2}$4), and (30$\bar{3}$0) TiF$_3$ diffraction rings indicate that the TiF$_3$ domains do not have any in-plane preferred orientation. A typical SAED pattern is shown in Fig. 7(b). The 0002 Ti diffraction ring emanates from untransformed portions of the Ti layer. The size of the TiF$_3$ domains are comparable to the average Ti grain size, 37 nm, in the as-deposited films, suggesting that TiF$_3$ formation proceeds within individual Ti grains. The interplanar spacings and the crystal structure of TiF$_3$ are nearly identical to those of hexagonal Ti$_2$O$_3$ (Ref. 30) which could also have formed during TEM sample preparation. Thus, in order to conclusively identify the second phase, further characterization was carried out by XRD and XPS.

Typical XRD diffractograms obtained from 250-nm-thick Ti samples exposed to WF$_6$ are reproduced in Figs. 9(a) and 9(b). Thicker samples were used to reduce the relative contribution of diffracted intensity from native surface oxides (angle-resolved RBS showed that oxygen was confined to the surface of the samples), and to obtain better signal-to-noise ratios for low-intensity peaks. The Ti(0002) and (10$\bar{1}$0) peaks at $2\theta = 38.4°$ and 34.6° are the only Bragg reflections obtained from as-deposited samples, indicating an (0002) texture. Diffractograms obtained following WF$_6$ exposure contain additional Bragg peaks due to TiF$_3$ formation,
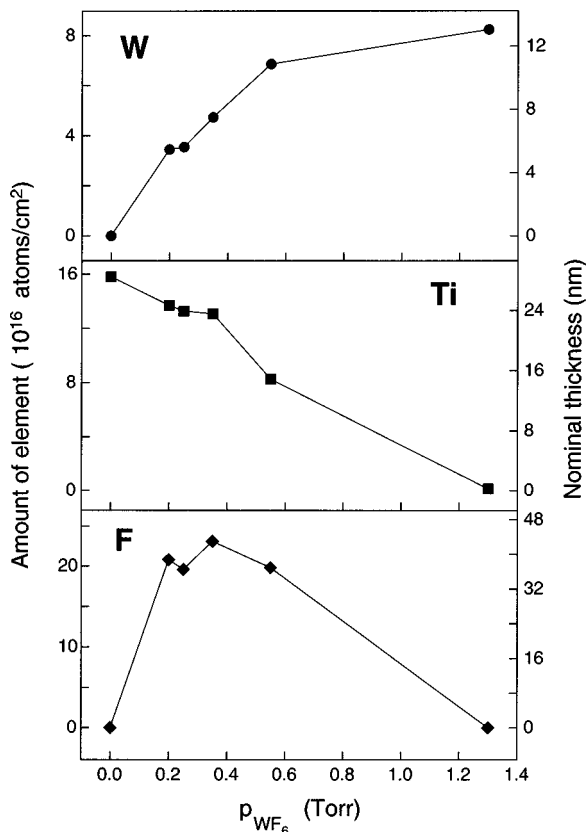

FIG. 5. The concentrations and nominal thicknesses of (a) W, (b) Ti, and (c) F in Ti/SiO$_2$ samples as a function of p_{WF_6}. The data were obtained by fitting RBS spectra using RUMP computer simulations.
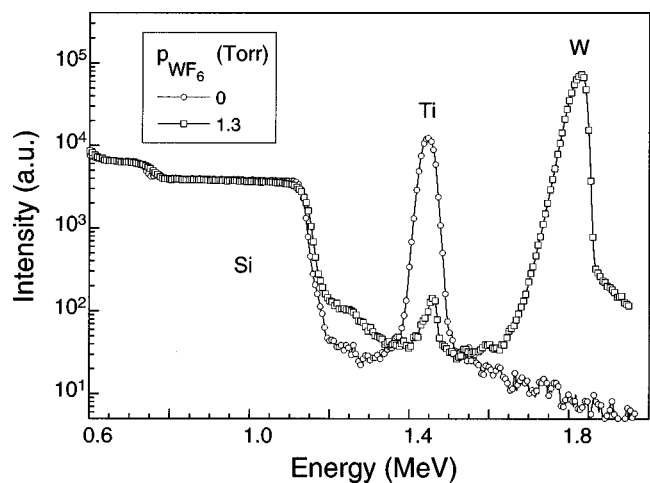

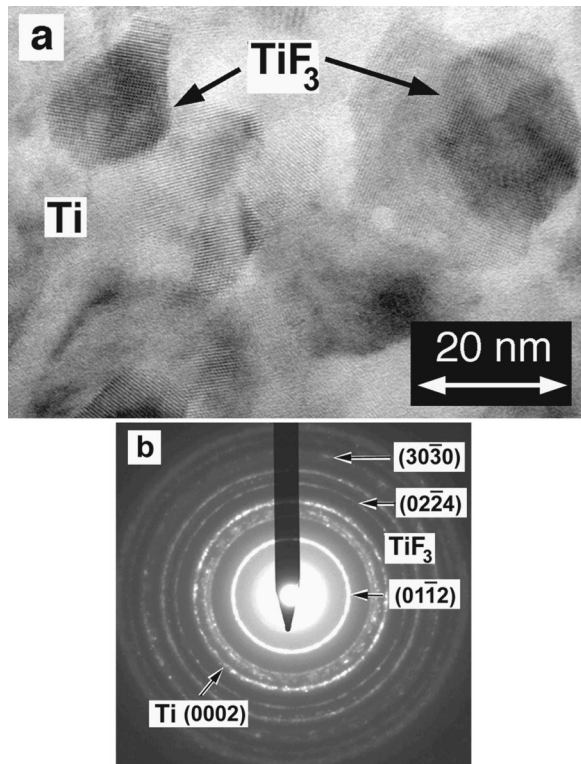FIG. 6. RBS spectra from Ti/SiO$_2$ samples prior to and following WF$_6$ exposure at $p_{WF_6} = 1.3$ Torr.

FIG. 7. (a) Typical plan-view HRTEM micrograph of a Ti sample exposed to WF$_6$ at $p_{WF_6} = 0.2$ Torr. TiF$_3$ domains are dispersed in the Ti film. (b) A SAED diffraction pattern showing $(01\bar{1}2)$, $(02\bar{2}4)$, and $(30\bar{3}0)$ diffraction rings from the TiF$_3$ domains.

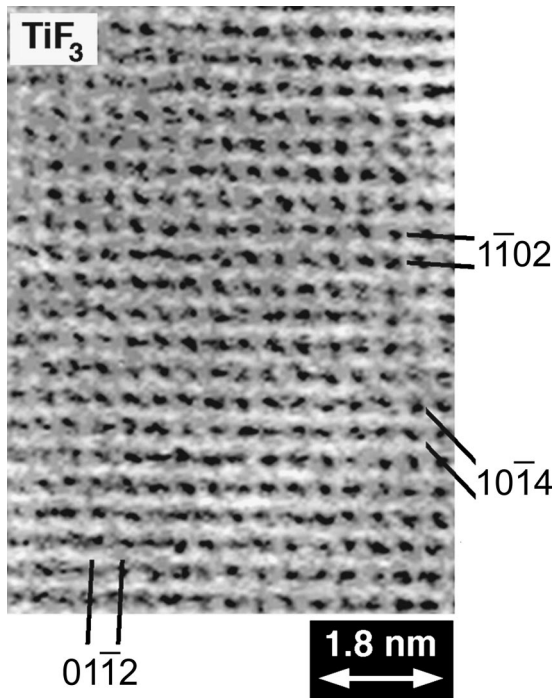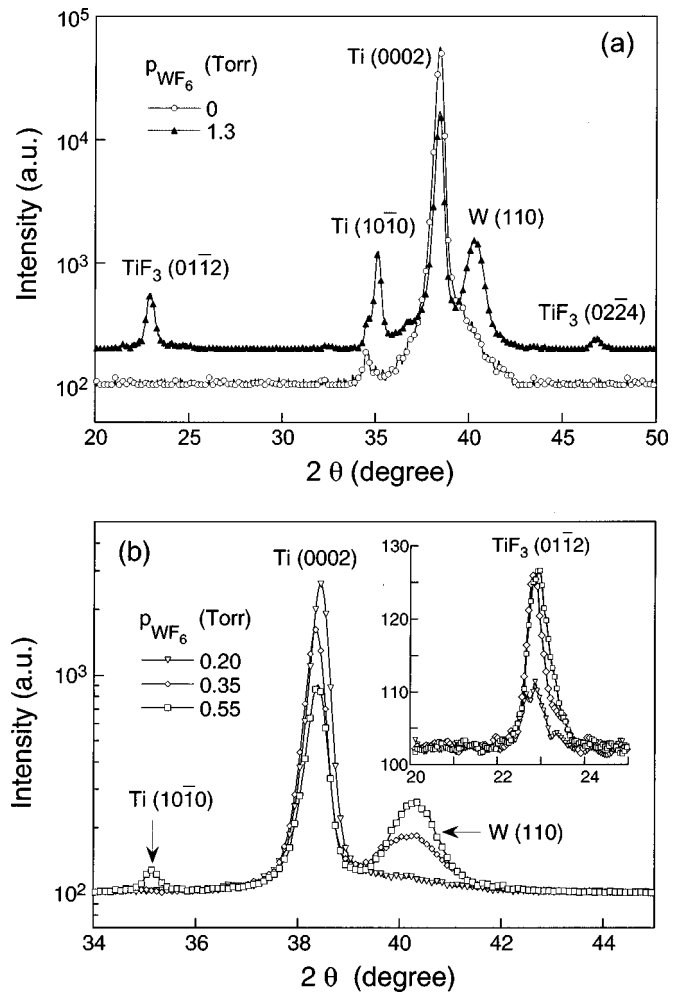FIG. 9. Typical XRD diffractograms obtained from (a) a 250-nm-thick as-deposited Ti sample and one exposed to WF$_6$ for 6 s at $p_{WF_6} = 1.3$ Torr; (b) samples exposed to WF$_6$ at intermediate p_{WF_6} values of 0.20, 0.35, and 0.55 Torr. The diffractogram of the WF$_6$ exposed sample in (a) is offset for clarity. Note that the intensity is plotted on a log scale.

FIG. 8. A $[20\bar{2}\bar{1}]$ zone axis HRTEM micrograph showing the atomic arrangement in the interior of one of the hexagonal TiF$_3$ domains in Fig. 7. Three sets of low index planes, $(01\bar{1}2)$, $(1\bar{1}02)$, and $(10\bar{1}4)$ are labeled.

$(01\bar{1}2)$ and $(02\bar{2}4)$ at $2\theta = 22.9°$ and $46.8°$, and bcc W deposition, (110) at $2\theta = 40.3°$.

Comparisons of relative intensities of the TiF$_3$ peaks with tabulated powder diffraction data reveal that TiF$_3$ grows with a $(01\bar{1}2)$ texture. Figure 9(b) shows that increasing p_{WF_6} to 0.55 Torr results in an increase in the TiF$_3$ $(01\bar{1}2)$ peak intensity with a simultaneous decrease in the Ti(0002) peak intensity. The Ti$(10\bar{1}0)$ peak intensity, which was barely detectable in the as-deposited sample [Fig. 9(a)], increases abruptly for exposures at $p_{WF_6} \geqslant 0.55$ Torr. We attribute the latter, as well as the shift in the $10\bar{1}0$ Ti peak to higher angles, to the delamination of the Ti layer which brings the $(10\bar{1}0)$ planes into Bragg alignment. An alternative explanation for the increase in the peak intensity would require the preferential growth of $(10\bar{1}0)$-oriented Ti grains at 445 °C. This is unlikely, however, since grain growth is expected to be insensitive to p_{WF_6}, whereas the observed change is abrupt and occurs only at high WF$_6$ exposures.

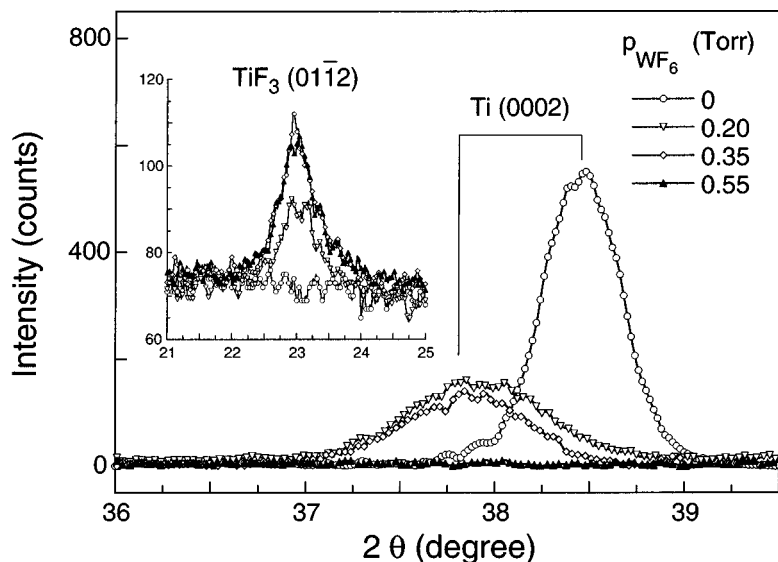Figure 10(a) shows XRD diffractograms obtained in the vicinity of the Ti(0002) peak, $2\theta = 38.47°$, from 27-nm-

FIG. 10. Typical XRD diffractograms from 27-nm-thick Ti films showing the Ti(0002) peak before and after WF_6 exposure for 6 s at various p_{WF_6} values. The inset shows a weak TiF_3 ($01\bar{1}2$) reflection observed in WF_6-exposed samples with $p_{WF_6} \leqslant 0.55$ Torr.

thick Ti samples exposed to WF_6 at different partial pressures. Raising p_{WF_6} from 0 to 0.20 Torr resulted in an increase in the (0002) Ti interplanar spacing from 0.234 to 0.238 nm due to F incorporation. The Ti(0002) peak position remains constant at 37.77 ° 2θ with further increases in p_{WF_6} indicating that the Ti layer is already saturated with F at partial pressures $\leqslant$ 0.2 Torr. Diffractograms obtained with extended counting times from WF_6-exposed Ti/SiO_2 samples show weak $01\bar{1}2$ TiF_3 diffraction peaks at $2\theta \approx 23$ ° (inset in Fig. 10). While the TiF_3 peak intensity increases when p_{WF_6} is raised to 0.35 Torr, it decreases with further WF_6 exposure at $p_{WF_6} = 0.55$ Torr, and disappears completely at 1.3 Torr. Ti, in these thinner samples, is no longer detectable by XRD following exposures to WF_6 at partial pressures > 0.35 Torr. Since Ti etching was not appreciable at $p_{WF_6} \approx 0.35$ Torr, observation of TiF_3 diffraction peaks in both thick and thin reacted Ti layers indicates the decrease in the Ti(0002) peak intensity is due to TiF_3 formation. The decrease in the TiF_3 peak intensity, together with the disappearance of the Ti(0002) peak at $p_{WF_6} > 0.35$ Torr, suggests that the entire (initially 27-nm-thick) Ti layer is transformed to TiF_3 at these WF_6 partial pressures.

In order to determine F depth distributions in Ti, the chemical state of Ti, and to distinguish TiF_3 from TiF_xO_y compounds, XPS measurements were carried out on Ti films before and after WF_6 exposure at 0.2 Torr. The W overlayer was removed from the WF_6 exposed samples by wet-chemical etching in $K_3Fe(CN)_6$ prior to XPS analyses. Spectra I and II in Fig. 11(a) show Ti $2p$ XPS peaks obtained from as-deposited and WF_6-exposed samples, respectively. Spectra III and IV were obtained after removing the native oxide by sputter etching using 5 keV Ar^+ ions. The corresponding F $1s$ spectra are in Fig. 11(b). The Ti $2p_{3/2}$ binding energy for the as-deposited sample was $\approx$ 458.9 eV. This agrees very well with Ti $2p_{3/2}$ peak positions obtained from commercially synthesized Ti_2O_3 and TiO_2. Spectrum II in Fig. 11(a) shows that the Ti $2p_{3/2}$ binding energy for the WF_6-exposed sample was slightly higher at $\approx$ 459.4 eV. This

increase in the metal binding energy results from the presence of residual amounts of electronegative F as indicated by the emergence of the F $1s$ peak in spectrum II, Fig. 11(b).

Removal of the surface oxide in the as-deposited sample resulted in a decrease in the Ti $2p_{3/2}$ binding energy to $\approx$ 454.1 eV, the expected peak position for pure Ti, as shown by spectrum III in Fig. 11(a). The sputter-etched WF_6-exposed sample, spectrum IV in Fig. 11(a), exhibited three overlapping Ti $2p$ peaks with maxima at $\approx$ 454.1, 461.2, and 467.1 eV. This is accompanied by a significant increase in the F concentration as shown by the corresponding spectrum IV in Fig. 11(b). Comparison of experimental data with simulated spectra obtained using PHI 5000 series ESCA software showed that the Ti $2p$ triplet arises from three distinct sets of chemical states (see Fig. 12). The main component of the highest-intensity central peak of the triplet is centered at 461.4 eV, which is identical to the Ti $2p_{3/2}$ binding energy measured from commercially synthesized TiF_3 samples. The Ti $2p_{1/2}$ peak from pure Ti, and a low intensity Ti $2p_{3/2}$ peak at 458.2 eV arising from the presence of a small amount of Ti oxide also contribute to the central peak. The high binding energy peak at 467.1 eV is the Ti $2p_{1/2}$ component from TiF_3, while the low energy peak at 454.1 eV is primarily due to the Ti $2p_{3/2}$ component from pure Ti.

The XPS results combined with the diffraction data above conclusively demonstrate that the major nonvolatile F-containing compound formed upon exposing Ti to WF_6 is TiF_3. The overall reaction path leading to compound formation at low p_{WF_6} exposures can be expressed as

$$2WF_6(g) + 4Ti(s) \rightarrow 2W(s) + 4TiF_3(s). \tag{1}$$
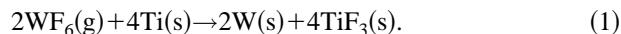
From tabulated thermochemical data,[31] the calculated Gibbs free energy change for reaction (1) at 445 °C is $\Delta G = -8.7$ eV, indicating that, in the absence of kinetic barriers, the reaction will proceed to the right.
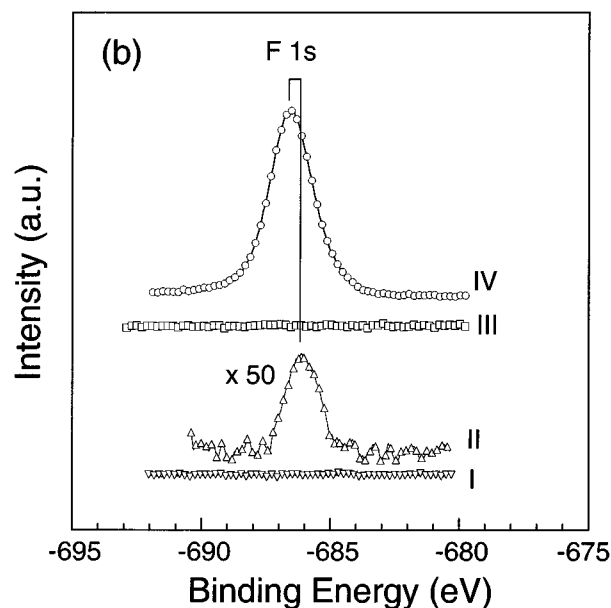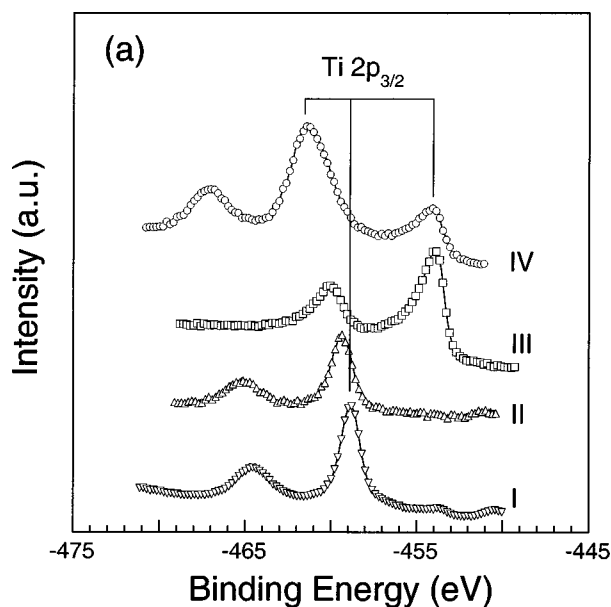
FIG. 11. (a) Ti $2p$, and (b) F $1s$ XPS spectra. Spectra I and II are obtained from as-deposited and WF$_6$-exposed (p_{WF_6}=0.2 Torr) Ti samples, respectively, prior to the removal of the native oxide. Spectra III and IV are obtained from the same samples after *in situ* removal of the native oxide by sputter etching.
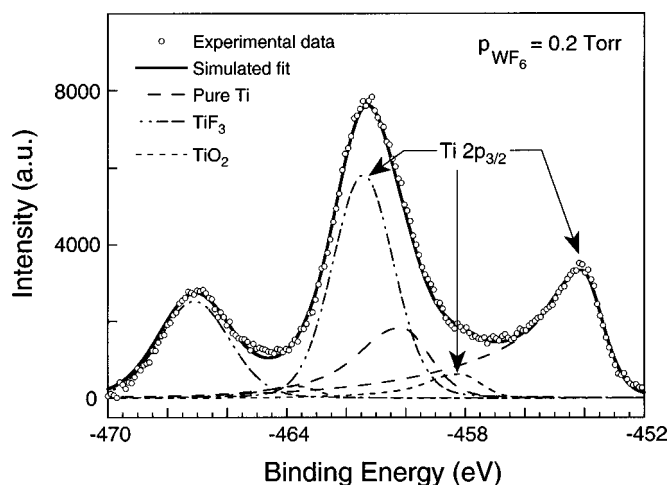

FIG. 12. Ti $2p$ XPS spectrum from WF$_6$-exposed (p_{WF_6}=0.2 Torr) Ti layers after the removal of the native oxide. The dashed curves show the deconvoluted components of the simulated spectrum used to fit the experimental data.

D. Volatile TiF$_4$ formation

The rapid etching of Ti by WF$_6$ at p_{WF_6}>0.35 Torr requires the evolution of a volatile Ti-containing compound. Since TiO$_x$, and TiW$_x$, and TiF$_3$ are not volatile at 445 °C,[32–34] and our RBS analyses suggest the evolution of a F-containing species at high p_{WF_6}, the feasibility of the TiF$_4$ formation was examined. The RBS results presented in Fig. 6 show that the amounts of Ti consumed and W deposited after WF$_6$ exposure at p_{WF_6}=1.3 Torr are (within 10% accuracy) 1.45×10^{17} and 8.25×10^{16} atoms/cm^2, respectively. Assuming that TiF$_x$ compound formation and W deposition occur by the reduction of WF$_6$ by the Ti film, x was esti-

mated by simple mass balance to be 3.4 ± 0.7, which is consistent with TiF$_4$ evolution. Thus, Ti reduction of WF$_6$ at high values of p_{WF_6} can be represented as

$$2WF_6(g)+3Ti(s)\rightarrow2W(s)+3TiF_4(g). \qquad (2)$$
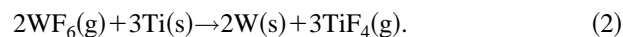
This reaction has a thermodynamic driving force ΔG $=-14.6$ eV at 445 °C.[31]

IV. DISCUSSION

A. W deposition by Ti reduction of WF$_6$

W deposition on Ti during WF$_6$ exposure occurs via chemisorption of impinging WF$_6$ molecules followed by a series of surface dissociation reactions. Since the precursor is F rich, the Ti surface is rapidly saturated with F. However, F diffusion into the Ti film is faster than F adsorption, exposing F-depleted Ti surfaces to the incident flux, thereby allowing further WF$_6$ reduction until a continuous W layer is formed. This is seen from our RBS results showing that the ratio of F in the Ti film to deposited W is ≈6 at low exposures, indicating that essentially all F diffuses into the Ti film. This interpretation is also corroborated by the XPS depth profiling results showing a low surface F concentration and is consistent with the absence of appreciable TiF$_4$ evolution at low WF$_6$ exposures.

We propose that further W deposition is facilitated by microcracking and delamination of the initially continuous W overlayer due to residual stresses generated near the W/Ti interface at local regions of high F concentration. Development of residual stresses due to F incorporation is indicated by our XRD results showing the expansion of the hcp Ti lattice due to Ti–F solid solution formation, and a 230% volume expansion of the primitive unit cell[29,35] occurring during the Ti→TiF$_3$ transformation. Microcracks expose portions of the Ti layer with relatively low F content, promoting WF$_6$ reduction and local growth of W particles, and increasing the local F concentration. Thus, new W/Ti interfaces with higher F concentrations are created, leading to a cascad-

ing effect. The connection between stress-induced cracking of the W film and localized particle growth is supported by our SEM results which show enhanced particle growth around microcracks. This argument is also consistent with enhanced growth and microcracking observed at the edges of topological features which are expected to have high stress concentrations.

Our XPS results demonstrate that the presence of a thin native layer on Ti does not prevent W deposition. In fact, the oxide layer remains relatively intact even after enormous quantities, $\approx 2.0 \times 10^{17}$ atoms/cm^2, of F have penetrated through it. Thus, while the presence of a native Ti oxide may alter the reaction kinetics, it does not prevent WF$_6$ reduction. This is supported by the results of Lee and co-workers,[36] who have verified the feasibility of WF$_6$ reduction by TiO$_2$ leading to TiF$_4$ formation at temperatures above 300 °C.

B. Phase formation sequence

Our results demonstrate that the phase formation reaction path during WF$_6$ reduction by Ti depends strongly on the amount of WF$_6$ exposure, and provides a basis for understanding the conflicting reports of previous studies.[19,20,22–24] At low WF$_6$ exposures, $p_{WF_6} < 0.2$ Torr, F rapidly diffuses into the Ti film and forms a solid solution. F dissolved in Ti expands the hcp lattice as indicated by an increase in the Ti(0002) interplanar separation. The presence of untransformed Ti grains together with TiF$_3$ domains as shown by our TEM results when the F/Ti ratio is < 3, is consistent with the dissolution of F in Ti at low p_{WF_6} values. TiF$_3$ formation is expected to occur by the reaction of Ti–F solid solution with incident WF$_6$ in regions with a large population of microcracks near the W/Ti interface. As WF$_6$ reduction proceeds and the average F concentration in the Ti film continues to increase, entire Ti–F grains are transformed into TiF$_3$. The columnar arrangement of F between Ti atoms in the TiF$_3$ unit cell when viewed along the (0002) zone axis, and the small atomic size of F compared with the interatomic spacings in the Ti lattice, suggest that F diffuses through interstitial sites in the highly (0002) textured Ti film.

High WF$_6$ exposures, $p_{WF_6} > 0.35$ Torr, cause fluorination of TiF$_3$, resulting in TiF$_4$ evolution. This reaction path, TiF$_4$ formation by the consumption of TiF$_3$, is indicated by the concurrent decrease in TiF$_3$ XRD and Ti RBS and XRD peak intensities observed in thin Ti samples exposed at $p_{WF_6} > 0.35$ Torr. The persistence of the Ti(0002) XRD peak until just prior to the onset of Ti etching ($p_{WF_6} = 0.35$ Torr) shows that a Ti–F solid solution is present even when the nominal concentration in the Ti layer is high enough to form volatile TiF$_4$. Regions of low F concentration in the Ti film due to the local presence of an intact W overlayer with a low population of microcracks is the likely reason for the continuing presence of Ti–F solid solution at high WF$_6$ partial pressures.

The phase formation sequence outlined above can be understood as follows. Ti–F solid solution formation is energetically favored over titanium fluoride formation when C_F is small. F incorporation in Ti continues until C_F exceeds a critical value C_F^*, at which point the free energy of the sys-

tem is reduced by compound formation. The equilibrium solubility limit of F in Ti is not known. However, we estimate the lower limit of C_F^* in our experiments (which are far from equilibrium) to be ≈ 10 at. % based upon combined XRD, RBS, and SIMS analyses of WF$_6$-exposed TiN/Ti samples.[18]

While both TiF$_3$ formation and TiF$_4$ evolution are thermodynamically feasible when $C_F > C_F^*$, the reaction leading to TiF$_4$ formation has a larger driving force [see Eqs. (1) and (2)] than that causing TiF$_3$ formation. However, our results showing TiF$_3$ formation prior to TiF$_4$ evolution indicate that TiF$_3$ formation—by the fluorination of Ti–F solid solution— has a lower kinetic barrier. Thus, when C_F^* is exceeded at low WF$_6$ partial pressures, the Ti–F solid solution rapidly transforms to TiF$_3$, while at high WF$_6$ exposures, TiF$_4$ evolution occurs by the fluorination of TiF$_3$ through the reaction

$$\text{WF}_6(\text{g}) + 6\text{TiF}_3(\text{s}) \rightarrow \text{W}(\text{s}) + 6\text{TiF}_4(\text{g}), \qquad (3)$$
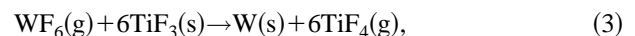
resulting in a free energy decrease $\Delta G = -3.1$ eV. TiF$_4$ evolution can also occur by this reaction pathway at low p_{WF_6} when WF$_6$ reacts with TiF$_3$ formed at local areas on the Ti surface. This explains the observation that small amounts of Ti are removed even at $p_{WF_6} < 0.35$ Torr.

C. Reaction mechanism and W morphology

The disappearance of the entire Ti film, despite the presence of a 120-nm-thick continuous W overlayer, can be understood based upon a phenomenological model illustrated schematically in Fig. 13. At low p_{WF_6}, TiF$_3$ formation in local areas near the W/Ti interface causes microcracking and delamination of the W overlayer. The impinging WF$_6$ molecules are reduced by the freshly exposed areas of Ti, leading to enhanced growth of W particles. With increasing WF$_6$ exposure, entire Ti grains are transformed to TiF$_3$. The large stresses developed at the Ti/SiO$_2$ interface due to TiF$_3$ formation, in addition to the displacement of the Ti–O and Ti–Si bonds (essential to maintain good adhesion) by Ti–F bonds weaken the interface resulting in local delamination of the Ti film. Elongated microcracks across the film and delaminated areas both provide access for WF$_6$ to penetrate the W film and attack the unreacted portions of the delaminated Ti film. Thus, W deposition proceeds from below as well (see Fig. 13). When most of the Ti layer has been converted to TiF$_3$, further WF$_6$ exposure results in the evolution of TiF$_4$ through the microcracks in the W film until the entire Ti layer is consumed, leaving behind a free standing W film which has extremely poor adhesion to the SiO$_2$ substrate.

V. CONCLUSIONS

WF$_6$ exposure to Ti leads to reduction and W deposition as F rapidly penetrates the Ti layer even when a Ti oxide is present on the surface. The primary Ti fluoride phase formed is determined by the WF$_6$ dose. At low WF$_6$ partial pressures, a Ti–F solid solution and a nonvolatile TiF$_3$ compound are formed. The large stresses generated by TiF$_3$ formation result in the formation of microcracks in the W film and delamination of the Ti layer at the Ti/SiO$_2$ interface. At high partial pressures, WF$_6$ continues to attack the underly-
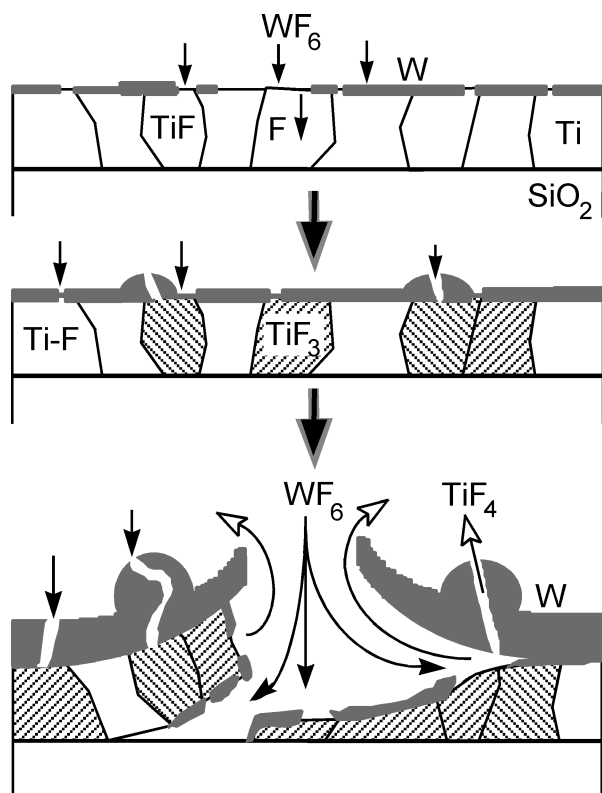
FIG. 13. Schematic representation of a phenomenological model depicting the sequence of reactions and morphological changes occurring in Ti/SiO$_2$ structures during WF$_6$ exposure. Unmarked closed arrows refer to WF$_6$, while open arrows connote TiF$_4$ evolution.

ing Ti layer by diffusing through the microcracks, etching the entire Ti film through the evolution of gaseous TiF$_4$, leaving behind a W film with extremely poor adhesion to the SiO$_2$ substrate.

ACKNOWLEDGMENTS

[1] T. Ohba, Appl. Surf. Sci. **91**, 1 (1995).

[2] S. L. Lantz, A. E. Bell, W. K. Ford, and D. Danielson, J. Vac. Sci. Technol. A **12**, 1032 (1994).

[3] E. J. McInerney, T. W. Mountsier, B. L. Chin, and E. K. Broadbent, J. Vac. Sci. Technol. B **11**, 734 (1993).

[4] S.-L. Zhang, R. Palmans, J. Keinonen, C. S. Petersson, and K. Maex, Appl. Phys. Lett. **67**, 2998 (1995).

[5] P. E. Riley, T. E. Clark, E. F. Gleason, and M. M. Garver, IEEE Trans. Semicond. Manuf. **3**, 150 (1990).

[6] R. P. Singh, K. W. Choi, R. Joshi, F. Dorleans, J. Estabil, and M. Lakritz, *Proceedings of Advanced Metallization for ULSI Applications* (Materials Research Society, Pittsburgh, 1991), Vol. 6, p. 153.

[7] G. Ruhl, B. Fröschle, P. Ramm, A. Intemann, and W. Pamler, Appl. Surf. Sci. **91**, 382 (1995).

[8] T. J. Licata, E. G. Colgan, J. M. E. Harper, and S. E. Luce, IBM J. Res. Dev. **39**, 419 (1995).

[9] M. L. Green and R. A. Levy, J. Electrochem. Soc. **132**, 1243 (1985).

[10] W. Gruenwald, S. E. Shulz, B. Hintze, and T. Gessner, Appl. Surf. Sci. **73**, 290 (1993).

[11] M. M. Farahani, J. F. Buller, B. T. Moore, and S. Garg, IEEE Trans. Semicond. Manuf. **7**, 79 (1994).

[12] A. Sakamoto, S. Chen, H. Tamura, M. Yoshimaru and M. Ino, Proceedings of the ninth IEEE VLSI Mult. Interconn. Conference, Santa Clara, 1991, p. 338.

[13] M. Rutten, D. Greenwell, S. Luce and R. Dreves, *Proceedings of Advanced Metallization for ULSI Applications*, edited by V. V. S. Rana, R. V. Joshi, and I. Ohdomari (Materials Research Society, Pittsburgh, 1992), Vol. 7, p. 277.

[14] A. Kohlhase, M. Mändl, and W. Pamler, J. Appl. Phys. **65**, 2464 (1989).

[15] G. Ramanath, J. R. A. Carlsson, J. E. Greene, L. H. Allen, V. C. Hornback, and D. J. Allman, Appl. Phys. Lett. **69**, 3179 (1996).

[16] G. Ramanath, J. E. Greene, J. R. A. Carlsson, L. H. Allen, V. C. Hornback, and D. J. Allman, Proceedings of VLSI Multilevel Interconnect Conference, Santa Clara, CA, 1997, Vol. 14, p. 246.

[17] G. Ramanath, V. C. Hornback, D. J. Allman, J. R. A. Carlsson, and L. H. Allen Proceedings of VLSI Multilevel Interconnect Conference, Santa Clara, CA, 1996, Vol. 13, p. 333.

[18] G. Ramanath, Ph.D. thesis, University of Illinois, Urbana, IL 1997.

[19] E. K. Broadbent, A. E. Morgan, J. M. DeBlasi, P. van der Putte, B. Coulman, B. J. Burrow, and D. K. Sadana, J. Electrochem. Soc. **133**, 1715 (1986).

[20] E. K. Broadbent, J. Vac. Sci. Technol. B **5**, 1661 (1987).

[21] E. K. Broadbent (private communication).

[22] M. L. Yu, Y. Ahn, and R. V. Joshi, J. Appl. Phys. **67**, 1055 (1990).

[23] M. L. Yu, Y. Ahn, and R. V. Joshi, IBM J. Res. Dev. **36**, 875 (1990).

[24] R. Barber and M. Shenasa, *Proceedings of the Seventh Workshop on Tungsten and Other Advanced Metals for ULSI Applications*, edited by G. Smith and R. Blumenthal (Materials Research Society Pittsburgh, 1990), p. 275.

[25] T. Moriya, S. Shima, Y. Hazuki, M. Chiba, and M. Kashiwagi, Tech. Dig. Int. Electron Devices Meet. **1973-7/83**, 550 (1983).

[26] N. Morita, T. Endo, T. Sato, and M. Shimada, J. Mater. Sci. Lett. **6**, 859 (1987).

[27] T. Endo, N. Morita, T. Sato, and M. Shimada, J. Mater. Res. **3**, 392 (1988).

[28] L. R. Doolittle, Nucl. Instrum. Methods Phys. Res. B **9**, 334 (1985); **15**, 227 (1986).

[29] S. Siegel, Acta Crystallogr. **9**, 684 (1956); JCPDS Powder Diffraction File #9-112.

[30] JCPDS Powder Diffraction File #43-1033.

[31] *JANAF Thermochemical Tables*, edited by W. W. Chase, C. A. Davies, J. R. Downey, D. J. Frurip, R. A. McDonald, and A. N. Syverud (National Bureau of Standards, 1985).

[32] *Phase Diagrams of Binary Titanium Alloys*, edited by J. L. Murray (ASM International, Metals Park, OH, 1987), p. 328.

[33] J. L. Murray and H. A. Wriedt, Bull. Alloy Phase Diagrams **8**, 148 (1987).

[34] R. J. H. Clark, in *Comprehensive Inorganic Chemistry*, edited by J. C. Bailar, H. J. Emeléus, R. Nyholm, and A. F. T. Dickenson (Pergamon, New York, 1973).

[35] JCPDS Powder Diffraction File #5-682.

[36] Y. H. Lee, C.-O. Park, D.-O. Kim, and J. S. Sun, J. Electron. Mater. **23**, 1075 (1994).